A Thermal Origin for Most Marsquakes

Zhang Lei[1], Zhang Jinhai[2], Mitchell Ross N[1], Cao Peng[3], and Liu Jihang[4]

[1]Institute of Geology and Geophysics, Chinese Academy of Sciences
[2]Institute of Geology and Geophysics, Chinese, Academy of Sciences
[3]Beijing University of Technology
[4]Bohai University

November 16, 2022

Abstract

The thermal response of the martian subsurface due to solar forcing lacks direct measurements. The InSight mission provides the best opportunity to detect the thermal behavior of the subsurface since it was equipped with both air temperature sensors and a subsurface heat flow probe. Here, we model heat conduction under the InSight landing site based on the measured subsurface thermal parameters and air temperature records, which provide insights into heat flow in the martian subsurface. Daily temperature variation over 1 K occurs only within 25 cm under the ground surface. The highest absolute rate of temperature change appears around sol 440, which coincides closely with the season of the dominant number of marsquakes observed around sunset. Thermal-mechanical finite-element method simulations indicate that more potential afternoon marsquakes might exist but be covered by the wind noise. Our results indicate that most high-frequency and low-magnitude marsquakes are likely thermal in origin.

A Thermal Origin for Most Marsquakes

Lei Zhang[1,2], Jinhai Zhang[1,2,3*], Ross N. Mitchell[4,5*], Peng Cao[6], Jihang Liu[7]

[1] Key Laboratory of Earth and Planetary Physics, Institute of Geology and Geophysics, Chinese Academy of Sciences, Beijing, China

[2] Innovation Academy for Earth Science, Chinese Academy of Sciences, Beijing, China

[3] College of Earth and Planetary Sciences, University of Chinese Academy of Sciences, Beijing, China

[4] State Key Laboratory of Lithospheric Evolution, Institute of Geology and Geophysics, Chinese Academy of Sciences, Beijing, China

[5] University of Chinese Academy of Sciences, Beijing, China

[6] College of Architecture and Civil Engineering, Beijing University of Technology, Beijing, China

[7] College of Control Science and Engineering, Bohai University, Jinzhou, Liaoning Province, China

[*]Corresponding authors: Jinhai Zhang (zjh@mail.iggcas.ac.cn) and Ross Mitchell (ross.mitchell@mail.iggcas.ac.cn)

Key Points:

- Daily and seasonal heat conduction under the InSight landing site is modeled.
- Daily temperature variation over 1 K occurs only within the depth of 25 cm.
- The highest absolute rate of temperature appears around sol 440, coincident with the dominant season of marsquakes observed around sunset.
- Thermal-mechanical simulations indicate that more potential afternoon marsquakes might exist but be covered by the wind noise.
- Most high-frequency and low-magnitude marsquakes are likely thermal in origin.

Abstract

The thermal response of the martian subsurface due to solar forcing lacks direct measurements. The InSight mission provides the best opportunity to detect the thermal behavior of the subsurface since it was equipped with both air temperature sensors and a subsurface heat flow probe. Here, we model heat conduction under the InSight landing site based on the measured subsurface thermal parameters and air temperature records, which provide insights into heat flow in the martian subsurface. Daily temperature variation over 1 K occurs only within 25 cm under the ground surface. The highest absolute rate of temperature change appears around sol 440, which coincides closely with the season of the dominant number of marsquakes observed around sunset. Thermal-mechanical finite-element method simulations indicate that more potential afternoon marsquakes might exist but be covered by the wind noise. Our results indicate that most high-frequency and low-magnitude marsquakes are likely thermal in origin.

Plain Language Summary

The mechanism of some marsquakes might not be tectonic in origin, but thermal, related to its large diurnal temperature difference. However, lack of comprehensive near-surface observation makes the thermal investigation challenging. We model the heat conduction beneath InSight based on the measured subsurface thermal parameters and air temperature records. Diurnal and seasonal variations of subsurface temperature and the rate of temperature change are analyzed. Daily temperature variations of >1 K only occur in the top 25 cm of the subsurface. In summer, the absolute rate of temperature change reaches its peak, which is also notably the dominant season of marsquakes observed around sunset. Thermal-mechanical simulations indicate that the heat-induced ground motion is evidently stronger in the daytime than that in the nighttime. Covered by the wind noise, more potential marsquakes might exist in the afternoon through the entire martian year. Our results indicate that high-frequency marsquakes are related to thermal conduction in the top 10 cm of the ground.

1 Introduction

The daily variation of temperature on Mars can reach up to 80–100 K [*Banfield et al.*, 2020]. Such a large thermal range can strongly influence both the weather variability and the thermal behavior of the subsurface. Satellite measurements can be used to estimate the thermal parameters from the ground surface to high altitudes [*Ahern et al.*, 2021; *Mellon et al.*, 2000], but they can only provide large-scale and intermittent observations. It is difficult to maintain a permanent weather station on the surface of Mars and to perform continuous underground observation, even though both are necessary for understanding the thermal behavior of subsurface materials. The InSight mission was equipped with both an air temperature gauge on the lander [*Spiga et al.*, 2018] and a deployable subsurface heat flow probe, the Heat Flow and Physical Properties Package (HP^3) [Spohn et al., 2018], which provides the best opportunity to detect the thermal behavior of subsurface materials due to the variation of near-surface temperature. The HP^3 mole successfully bored 20–30 cm deep [Good *et al.*, 2021] and performed direct detection on critical thermal parameters of the shallow martian subsurface.

Here, we perform a series of numerical simulations to infer the heat conduction process under the InSight landing site, based on the measured subsurface thermal parameters and the air temperature records. We further analyze the daily and seasonal variations of subsurface temperature and the rates of temperature change. Thermal-mechanical coupling finite-element simulations reveal the daily variation of the temperature and the strain in the subsurface. Our results indicate that underground heat conduction on Mars has been critically overlooked in the interpretation of marsquakes.

2 Diurnal and Seasonal Variations of the Subsurface Heat Conduction Beneath InSight

The heat conduction equation can describe the thermal process of a given model with several controlling parameters (Text S1). In our numerical calculations, we use typical values of these parameters obtained from the heating experiments from HP^3 [*Grott et al.*, 2021] as follows: soil density $\rho = 1211$ kg m^{-3}, specific heat $c = 630$ J kg^{-1} K^{-1}, and thermal conductivity $k = 0.039$ W m^{-1} K^{-1}. Thus, the thermal diffusivity $\kappa = k/(\rho c)$ at the InSight landing site can be estimated as 5.1×10^{-8} m^2 s^{-1}. The air temperature sensors are on the deck of the InSight lander, ~1 m over the ground. We correct the air temperature to the ground temperature according to the recorded air temperature and ground temperature from the Martian Climate Database [Forget *et al.*, 1999] (Text S2; Fig. S1). Daily subsurface heat conduction calculation results (Text S3; Fig. S2) for the annually average sol show that the ground surface (depth of 0 cm) reaches its highest temperature (~290 K) at ~15:00 local mean solar time (LMST) and drops to the lowest temperature (~180 K) slightly before ~06:00. In contrast, at a depth of ~3 cm, the highest temperature (~250 K) appears slightly after ~16:00 and drops to the lowest temperature (~195 K) slightly after ~06:00, yielding 1 hr and <1 hr time delays compared to the surface, respectively. At a depth of 7 cm, where the maximum daily variation is only ~15 K, the highest temperature appears at ~19:00 and the lowest temperature appears at ~11:00, yielding 4 hr and 5 hr time delays compared to the surface, respectively. Thus, time delays of the lowest and highest temperature (<1 hr cm^{-1}) can be seen at different depths. Diurnal temperature variations of over 1 K only occur within the top 25 cm. This indicates that we can focus on the shallowest 25 cm for analyzing the diurnal variations of subsurface temperature, especially for the shallowest 10 cm, below which daily temperature variations are less than 15 K.

Similar to the annually averaged data and model, we can further calculate the real-time heat field under the InSight landing site day by day with measured thermal parameters and daily ground temperature. Figure S3 presents the daily temperature at different depths in the first martian year after InSight landed. The daily ground temperature exhibits several characteristics, such as the lowest daily temperature at ~06:00 (around sunrise), the highest daily temperature at ~14:00, and the highest absolute rate of temperature change at ~18:00 (around sunset). Figure 1 presents the temperature profile at these moments for each sol. We mark a zone with temperature over ~230 K (black isolines) as the “hot zone” and the other as the “cold zone”. We can see that the “hot zone” at 14:00 has depths within 6 cm, varying from ~4 cm during sols 0–300 down to ~6 cm around sol 500 (Fig. 1b). At 18:00, the “hot zone” is deeper than that at 14:00, varying from ~6 cm in depth during sols 0–300 down to ~10 cm around sol 550 (Fig. 1c). In sols 230–610, the top of the “hot zone” is 2 cm in depth, which indicates dramatic increases of temperature in this zone.

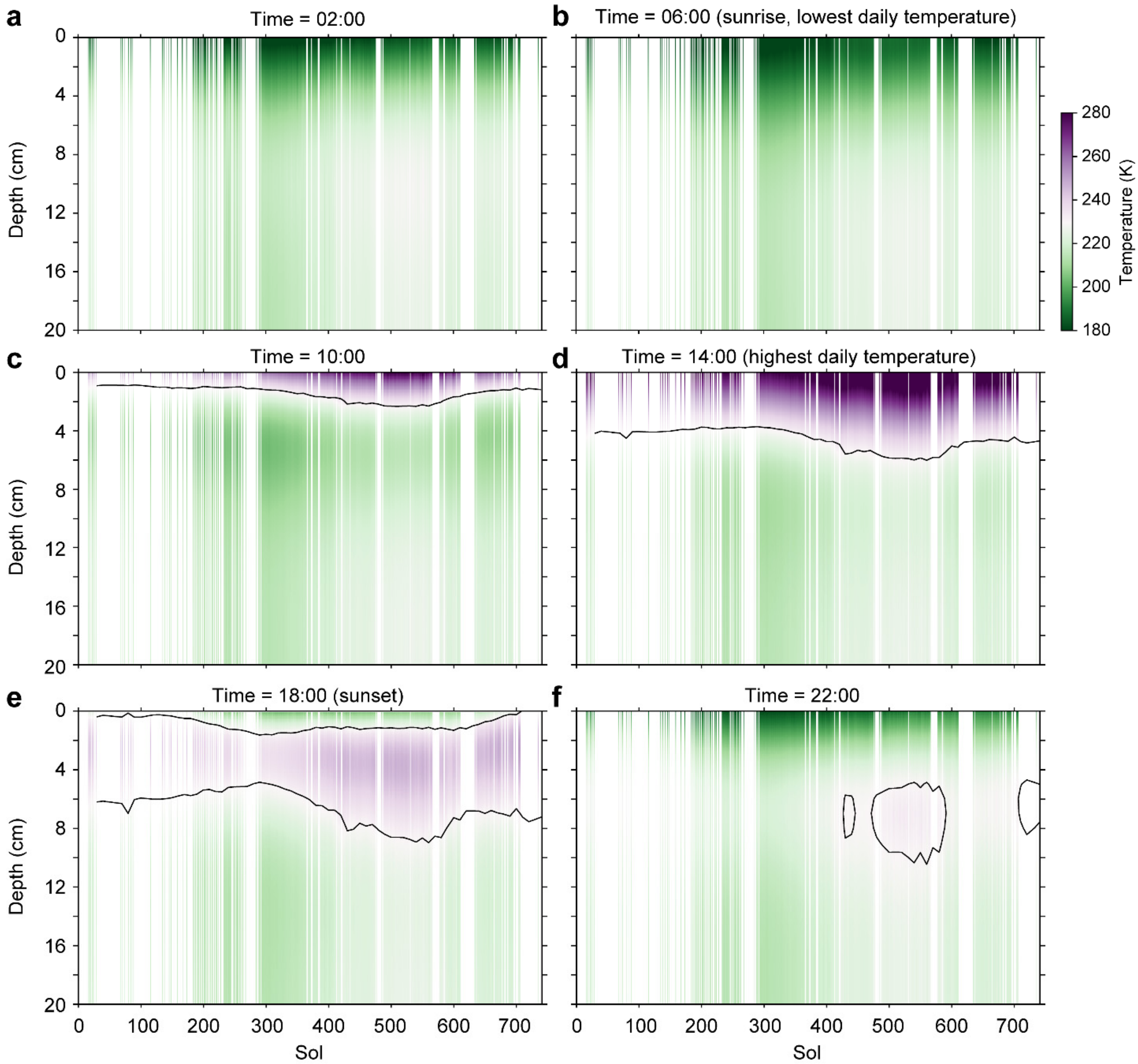

Figure 1. Temperature as a function of both depth and mission days (sol) at characteristic moments of day. Vertical white spaces indicate data gaps due to solar conjunctions or machine stoppages. Black lines denote the isolines of 230 K.

3 Correspondence Between Rate of Temperature Change and Ground Motion Around Sunset

Using seismic data recorded by InSight's seismic experiment for interior structure (SEIS) [*Lognonné et al.*, 2019] deployed on the ground at the InSight landing site, a number of marsquakes have been detected [*Ceylan et al.*, 2021; *Clinton et al.*, 2021; *Giardini et al.*, 2020]. Strikingly, the timing of marsquakes is highly non-uniform, with no observed diurnal or seasonal dependence (Fig. 2). About 49% of marsquakes occur within a 2 hr time window near sunset (17:00–19:00) and 70% of them occur within a 4 hr time window near sunset (16:00–20:00) (Table S1). Furthermore, nearly all the remaining minority of events occur at nighttime after sunset and twilight (Fig. S4). The strong wind noise precludes the detection of potential weak marsquake signals during the daytime or in the dust-storm season. Nevertheless, larger magnitude marsquakes, were they to occur during the windy daytime or dust-storm season, should still be detectable, thus making their absence conspicuous. That is, if large magnitude marsquakes are tectonic in origin, they should occur at more or less random times of day and year, assuming that tectonic marquakes are similar to earthquakes (e.g., *Hao et al.* [2019]). However, only several high quality marsquakes have been detected in an entire martian year [*Khan et al*., 2021], far lower than the frequency of moonquakes [*Garcia et al*. 2019].

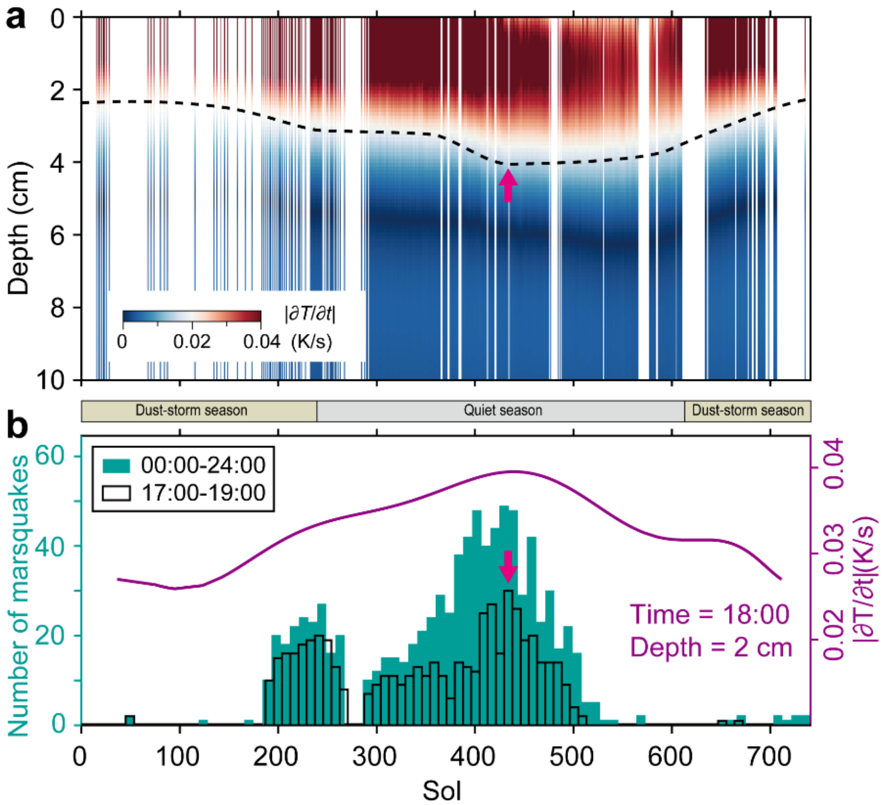

Figure 2. **Rate of temperature change and the ground motion around sunset.** (a) Comparison between the absolute rate of temperature variation at 18:00 LMST and number of events in high-frequency family (see below). The dashed line indicates the boundary of ~0.02 K s^{-1}. (b) Green filled and black framed bars indicate marsquakes during 00:00–24:00 LMST and 17:00–19:00 LMST, respectively. The purple line is the temperature variation at the depth of 2 cm at 18:00 LMST. Temperature variations at other depths are shown in Figure S5. Only marsquakes in the high-frequency family (HF, VHF, and SHF) [*InSight Marsquake Service*, 2021] are plotted. See all types of marsquakes in Figure S6.

It is well known that rapid temperature change can cause thermal expansion and contraction and even cracks in rock, which would change its mechanical properties. It has been suggested that marsquakes might be related to thermal cracking of the subsurface [*Dahmen et al.*, 2021], like thermal quakes on the tectonically dormant Moon [*Duennebier and Sutton*, 1974; *Sens-Schönfelder and Larose*, 2010]. Thus, based on our calculated temperature field and the

InSight marsquake catalog [*InSight Marsquake Service*, 2021], we analyze the correspondence between the seasonal variations in thermal conduction with the occurrences of marsquakes. Figure 2 shows the absolute rate of temperature change $|\partial T/\partial t|$ at 18:00 and the number of marsquake events in the high-frequency family [*InSight Marsquake Service*, 2021] during 17:00–19:00. This low-wind time window is the quietest, thus providing the most reliable record of marsquakes (Fig. S4).

It is evident that the absolute rate of temperature variation $|\partial T/\partial t|$ at 18:00 and the number of high-frequency events (high frequency (HF), very high frequency (VHF), and super high frequency (SHF)) are essentially synchronous during an entire martian year (except the dust-storm season), and both reach their peak values at around sol 440 (in summer). It is notable that marsquakes do not occur more frequently during the peak temperature (around sol 540); instead, they occur more frequently around sol 440, corresponding to the peak rate of temperature change. The absolute rate of temperature change on sol 440 was >0.02 K s^{-1} within a depth of ~4 cm (Fig. 2a). This indicates that high-frequency events might be related to thermal conduction within only the top several centimeters of the subsurface.

4 A Thermal Origin for Most Marsquakes Inferred from Thermal-mechanical Simulation

Given the low heat conductivity in the martian subsurface, the rock-filled soil with a depth of 50 cm is considered in the simulation. Thus, we use a 2D thermal-mechanical coupling finite-element model (50 cm×100 cm) for the subsurface profile (Fig. 3a). The displacement boundary condition along the side and bottom boundaries is set as fixed in the normal direction and free in the tangential direction. Given that the thermal conduction dominates mainly in the top 10 cm of the subsurface, the top boundary is set as a free surface with corrected ground temperature, while the side and bottom boundaries are set as adiabatic. For the soil at InSight landing site, the S wave velocity, P wave velocity [Hobiger *et al.*, 2021] and density [*Grott et al.*, 2021] are set as 111 m s^{-1}, 200 m s^{-1}, and 1211 kg m^{-3}, respectively; the thermal diffusivity is set as 5.1×10^{-8} m^2 s^{-1}, obtained from the measured thermal parameters [*Grott et al.*, 2021]; thermal expansion is set as 2.4×10^{-4} K^{-1} [Molaro *et al.*, 2017]. For the rocks buried in the soil (Fig. 3a), the S wave velocity, P wave velocity and density are set as 1700 m s^{-1}, 3000 m s^{-1}, and 2760 kg m^{-3} [Morgan *et al.*, 2018], respectively, derived from terrestrial data obtained for fractured basalt [Planke *et al.*, 1999]; thermal diffusivity is set as 7×10^{-7} m^2 s^{-1} [Hartlieb *et al.*, 2016]; the thermal expansion is set as 1×10^{-5} K^{-1} [Molaro *et al.*, 2017]; and the volume ratio of the filled rocks is set as approximately 5 %.

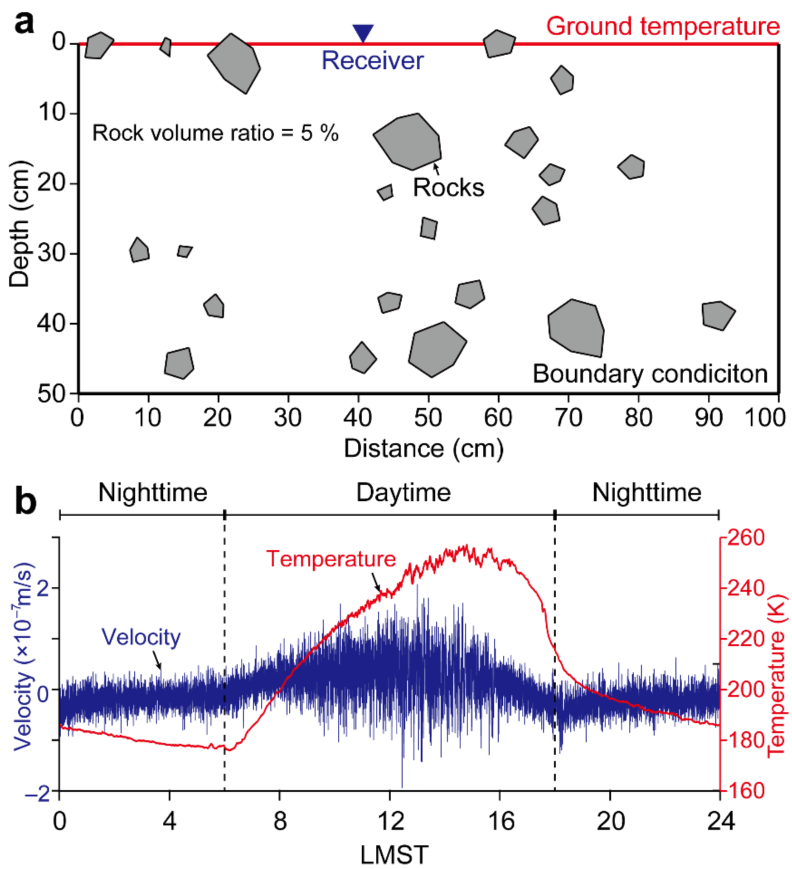

Figure 3. The 2D thermal-mechanical coupling finite-element model and the simulated ground motion. (a) The model with a depth of 50 cm and width of 100 cm. The polygons denote rocks in the soil and the reversed triangle on the ground denotes the receiver of seismic waves. (b) the input ground temperature, corrected from the InSight temperature record in sol 226 and the simulated ground motion (vertical velocity) at the receiver of seismic waves.

The results show that driven by the diurnal air temperature variation, the ground motion is evident and highly correlated with the magnitude of temperature changes. The amplitude of the vertical velocity is evidently larger in the daytime than that in the nighttime (Fig. 3b), which has similar trend with the measured vertical ground motion by InSight's SEIS. The peak ground acceleration of the simulated heat-induced (Fig. S7) is comparable to the average amplitude of high-frequency marsquake events identified by SEIS [*Ceylan et al.*, 2021] in the sunset (10^{-9} − 10^{-8} m s^{-2}), which indicates that the heat variation might be adequate to induce thermal marquakes.

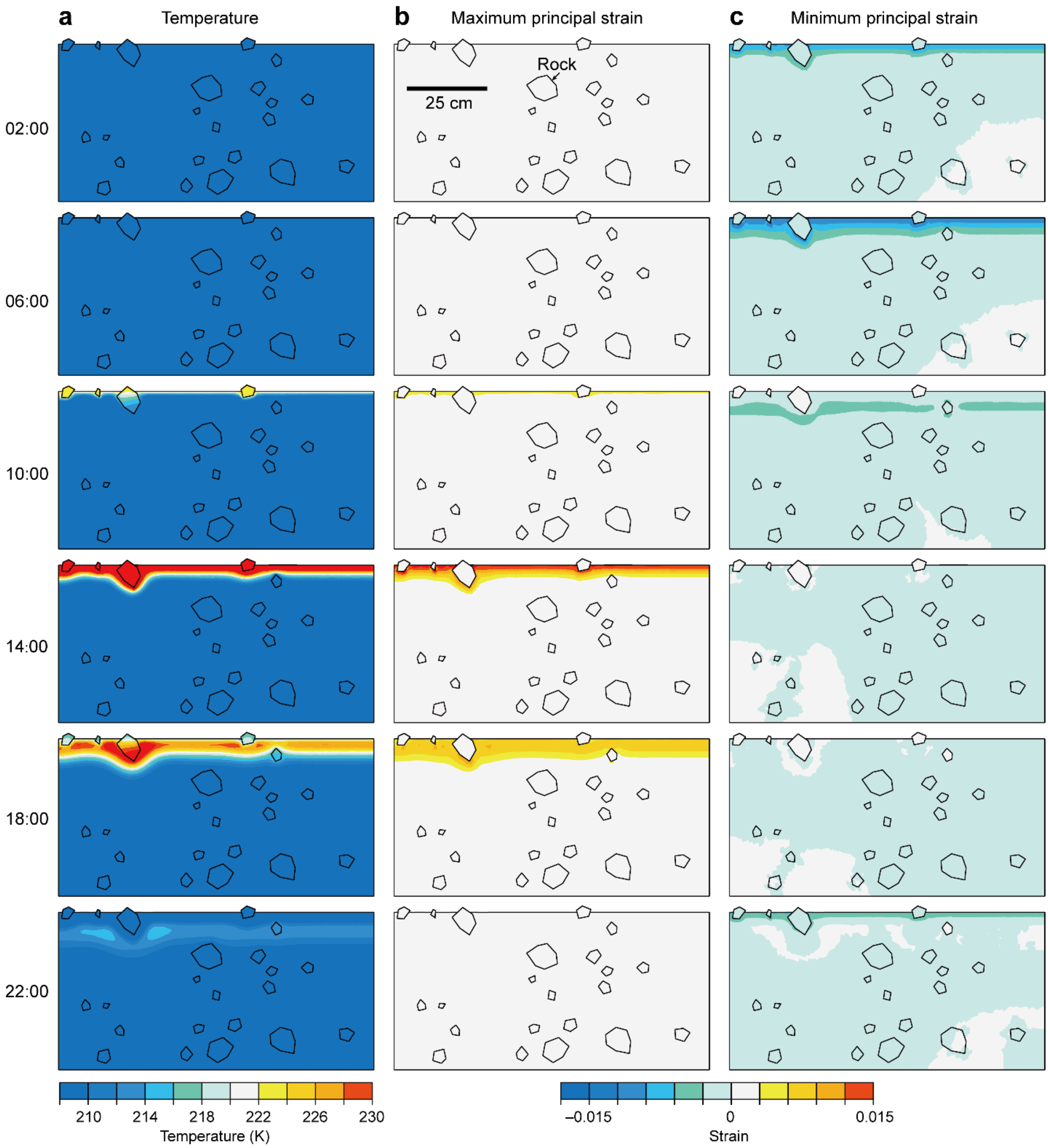

Figure 4. Representative snapshots of temperature and strain. (a) Temperature; (b) Maximum principal strain; (c) Minimum principal strain. The 6 rows from the top to the bottom denote the snapshots at 02:00, 06:00, 10:00, 14:00, 18:00 and 22:00 LMST, respectively.

Time-varying temperature distribution shows that the subsurface temperature varies mainly within the top ~ 10 cm and is strongly affected by the part-buried rocks (Fig. 4a). In the early morning (e.g., 02:00 and 06:00), the minimum principal strain (Fig. 4c) reaches its lowest values (~-0.01), which indicates that the subsurface is compressed due to low temperature. In the afternoon (e.g., 14:00 and 18:00), the maximum principal strain (Fig. 4b) reaches its peak values (~0.01) in the top ~10 cm, which indicates the failure or fracture of the subsurface. This is consistent with the frequently recorded sunset marsquakes. This indicates that more potential afternoon marsquakes might exist but be covered by wind noise before the sunset (e.g., 14:00), during which the maximum strain is even higher than that in the sunset.

5 Discussions

We simulated the ground motion induced by daily temperature variation in the subsurface. The amplitude of simulated acceleration is ~5×10^{-8} m s^{-2} in the representative sol (Fig. S7), which is much smaller than that of the observed acceleration by SEIS (< 10%) in the same sol. However, their trends are basically consistent, which are strong in the daytime but weak in the nighttime. These indicate that other sources (e.g., wind) besides temperature variation might dominate the surface ground motion. If the wind was further considered in the simulation, the heat-induced ground motion would be exaggerated and gain a higher amplification on the amplitude of acceleration. More work is needed in the future by considering the coupling process between thermal activity and wind shaking.

Our current experiments show that the marsquakes occur at the zone with high strainin the subsurface. Given that the sunset is away from the highest rate of temperature change in the sol, we expect that more potential thermal quakes may exist at the other time periods (such as 14:00-16:00 LMST, Fig. 4). However, the wind noise in these times is too strong to detect the weak signals.

6 Conclusions

Taking the ground temperature and subsurface heat properties observed by InSight as boundary conditions, we performed a series of numerical simulations based on heat conduction equation. From the analyses of subsurface temperature and the rate of temperature change, we infer that the depth of daily temperature variation over 1 K occurs only within 25 cm under the ground surface. This indicates that the strong daily temperature variation (up to 80–100 K) has little influence on the underground materials below this depth. Peak absolute rate of temperature change appears around sol 440 (in summer), which is strikingly coincident with the peak number of marsquakes observed starting at sunset. This temporal correspondence may suggest that the highest absolute rate of temperature change triggers thermal marsquakes. We infer that the thermal marsquakes mainly happen at the depth of <10 cm, over the zone of daily temperature variation with a threshold as little as 15 K, especially at the uppermost several centimeters with absolute rate of temperature change >0.02 K s^{-1}. Thermal-mechanical finite-element method simulations indicate that the heat-induced ground motion is evidently stronger in the daytime than that in the nighttime. In the afternoon, the maximum principal strain reaches its peak values in the top ~10 cm of the subsurface, which indicates the failure or fracture of the subsurface. The peak ground acceleration of the simulated heat-induced is comparable to the average amplitude of high-frequency marsquake events identified by SEIS in the sunset, indicating that these marquakes might have thermal in origin.

Acknowledgments

The TWINS (Temperature and Winds for InSight) datasets were downloaded from the NASA Planetary Data System [Rodriguez-Manfredi, *et al*. 2019]. The Marsquake catalog was obtained from IRIS [InSight Mars SEIS Data Service, 2019]. Computing resources were provided by The Supercomputing Laboratory at the Institute of Geology and Geophysics, Chinese Academy of Sciences (IGGCAS). This work was supported by National Natural Science Foundation of China (41941002 and 41888101). Comments and suggestions from Brian Shiro highly improved the manuscript. We thank Xiaofeng Liang for helpful discussions on daily temperature response of a seismometer deployed in the Taklimakan Desert.

References

Ahern, A. A., A. D. Rogers, C. S. Edwards, and S. Piqueux (2021), Thermophysical properties and surface heterogeneity of landing sites on Mars from overlapping Thermal Emission Imaging System (THEMIS) observations, *Journal of Geophysical Research: Planets*, *126*(6), e2020JE006713.

Banfield, D., A. Spiga, C. Newman, F. Forget, M. Lemmon, R. Lorenz, N. Murdoch, D. Viudez-Moreiras, J. Pla-Garcia, and R. F. Garcia (2020), The atmosphere of Mars as observed by InSight, *Nature Geoscience*, *13*(3), 190-198.

Barlow, N. (2014), Mars: An introduction to its interior, surface and atmosphere, *Mars: An Introduction to its Interior*, Cambridge University Press.

Ceylan, S., J. F. Clinton, D. Giardini, M. Böse, C. Charalambous, M. van Driel, A. Horleston, T. Kawamura, A. Khan, and G. Orhand-Mainsant (2021), Companion guide to the marsquake catalog from InSight, Sols 0–478: Data content and non-seismic events, *Physics of the Earth and Planetary Interiors*, *310*, 106597.

InSight Marsquake Service (2021). Mars Seismic Catalogue, InSight Mission; V7 2021-07-01. ETHZ, IPGP, JPL, ICL, Univ. Bristol. https://doi.org/10.12686/a12.

Clinton, J. F., S. Ceylan, M. van Driel, D. Giardini, S. C. Stähler, M. Böse, C. Charalambous, N. L. Dahmen, A. Horleston, and T. Kawamura (2021), The Marsquake catalogue from InSight, sols 0–478, *Physics of the Earth and Planetary Interiors*, *310*, 106595.

Dahmen, N. L., J. F. Clinton, S. Ceylan, M. van Driel, D. Giardini, A. Khan, S. C. Stähler, M. Böse, C. Charalambous, and A. Horleston (2021), Super high frequency events: A new class of events recorded by the InSight seismometers on Mars, *Journal of Geophysical Research: Planets*, *126*(2), e2020JE006599.

Duennebier, F., and G. H. Sutton (1974), Thermal moonquakes, *Journal of Geophysical Research*, *79*(29), 4351-4363.

Forget, F., F. Hourdin, R. Fournier, C. Hourdin, O. Talagrand, M. Collins, S. R. Lewis, P. L. Read, and J. P. Huot (1999), Improved general circulation models of the Martian atmosphere from the surface to above 80 km, *Journal of Geophysical Research: Planets*, *104*(E10), 24155-24175.

Garcia, R. F., et al. (2019), Lunar seismology: An update on interior structure models, *Space Sci Rev*, *215*(8). https://doi.org/10.1007/s11214-019-0613-y.

Giardini, D., P. Lognonné, W. B. Banerdt, W. T. Pike, U. Christensen, S. Ceylan, J. F. Clinton, M. van Driel, S. C. Stähler, and M. Böse (2020), The seismicity of Mars, *Nature Geoscience*, *13*(3), 205-212.

Good, A., A. Johnson, and G. Hautaluoma (2021), NASA InSight's 'Mole' ends its journey on Mars, in *https://www.nasa.gov/feature/jpl/nasa-insight-s-mole-ends-its-journey-on-mars*, accessed 4 Jan 2021.

Grott, M., T. Spohn, J. Knollenberg, C. Krause, T. L. Hudson, S. Piqueux, N. Müller, M. P. Golombek, C. Vrettos, and E. Marteau, et al., (2021), Thermal conductivity of the martian soil at the InSight landing site from HP^3 active heating experiments, *Journal of Geophysical Research: Planets*, 126(7), e2021JE006861.

Hartlieb, P., M. Toifl, F. Kuchar, R. Meisels, and T. Antretter (2016), Thermo-physical properties of selected hard rocks and their relation to microwave-assisted comminution, *Minerals Engineering*, *91*, 34-41.

Hao, J., J. Zhang, and Z. Yao (2019), Evidence for diurnal periodicity of earthquakes from midnight to daybreak, *National Science Review*, *6*(5), 1016-1023.

Hobiger, M., M. Hallo, C. Schmelzbach, S. Stähler, D. Fäh, D. Giardini, M. Golombek, J. Clinton, N. Dahmen, and G. Zenhäusern (2021), The shallow structure of Mars at the InSight landing site from inversion of ambient vibrations, *Nature communications*, *12*(1), 1-13.

InSight Mars SEIS Data Service. (2019). SEIS raw data, Insight Mission. IPGP, JPL, CNES, ETHZ, ICL, MPS, ISAE-Supaero, LPG, MFSC. https://doi.org/10.18715/seis.insight.xb_2016.

Khan, A., S. Ceylan, M. van Driel, D. Giardini, P. Lognonné, H. Samuel, N. C. Schmerr, S. C. Stähler, A. C. Duran, and Q. Huang (2021), Upper mantle structure of Mars from InSight seismic data, *Science*, *373*(6553), 434-438.

Lognonné, P., W. B. Banerdt, D. Giardini, W. Pike, U. Christensen, P. Laudet, S. De Raucourt, P. Zweifel, S. Calcutt, and M. Bierwirth (2019), SEIS: Insight's seismic experiment for internal structure of Mars, *Space Science Reviews*, *215*:12. https://doi.org/10.1007/s11214-018-0574-6.

Mellon, M. T., B. M. Jakosky, H. H. Kieffer, and P. R. Christensen (2000), High-resolution thermal inertia mapping from the Mars global surveyor thermal emission spectrometer, *Icarus*, *148*(2), 437-455.

Molaro, J. L., S. Byrne, and J.-L. Le (2017), Thermally induced stresses in boulders on airless body surfaces, and implications for rock breakdown, *Icarus*, *294*, 247-261.

Morgan, P., M. Grott, B. Knapmeyer-Endrun, M. Golombek, P. Delage, P. Lognonné, S. Piqueux, I. Daubar, N. Murdoch, and C. Charalambous (2018), A pre-landing assessment of regolith properties at the InSight landing site, *Space Science Reviews*, *214*(6), 1-47.

Rodriguez-Manfredi, J.A. et al. (2019), InSight APSS TWINS Data Product Bundle, NASA Planetary Data System, https://doi.org/10.17189/1518935.

Spohn, T., M. Grott, S. Smrekar, J. Knollenberg, T. Hudson, C. Krause, N. Müller, J. Jänchen, A. Börner, and T. Wippermann (2018), The heat flow and physical properties package (HP 3) for the InSight mission, *Space Science Reviews*, *214*(5), 1-33.

Planke, S., E. Alvestad, and O. Eldholm (1999), Seismic characteristics of basaltic extrusive and intrusive rocks, *The Leading Edge*, *18*(3), 342-348.

Sens-Schönfelder, C., and E. Larose (2010), Lunar noise correlation, imaging and monitoring, *Earthquake Science*, *23*(5), 519-530.

Spiga, A., D. Banfield, N. A. Teanby, F. Forget, A. Lucas, B. Kenda, J. A. R. Manfredi, R. Widmer-Schnidrig, N. Murdoch, and M. T. Lemmon (2018), Atmospheric science with InSight, *Space Science Reviews*, *214*(7), 1-64.

Geophysical Research Letters

Supporting Information for

A Thermal Origin for Most Marsquakes

Lei Zhang[1, 2], Jinhai Zhang[1, 2, 3*], Ross N. Mitchell[4,5*], Peng Cao[6], Jihang Liu[7]

[1] Key Laboratory of Earth and Planetary Physics, Institute of Geology and Geophysics, Chinese Academy of Sciences, Beijing, China
[2] Innovation Academy for Earth Science, Chinese Academy of Sciences, Beijing, China
[3] College of Earth and Planetary Sciences, University of Chinese Academy of Sciences, Beijing, China
[4] State Key Laboratory of Lithospheric Evolution, Institute of Geology and Geophysics, Chinese Academy of Sciences, Beijing, China
[5] University of Chinese Academy of Sciences, Beijing, China
[6] College of Architecture and Civil Engineering, Beijing University of Technology, Beijing, China
[7] College of Control Science and Engineering, Bohai University, Jinzhou, Liaoning Province, China

Contents of this file

Introduction

Text S1 gives the solution of 1D heat conduction equation.
Text S2 shows the process of the temperature correction from the air to the ground.
Text S3 analyses the results of the subsurface heat conduction beneath InSight.
Figure S1 presents the correction process from the air temperature to ground temperature.
Figure S2 shows the annually averaged heat conduction model of the subsurface under the InSight landing site.
Figure S3 shows the temperature as a function of both time of day and mission days (sol) at top 10 cm of the subsurface.
Figure S4 shows phase arrival times of the 6 types of marsquake events and their histogram.
Figure S5 shows the rates of temperature change at different depths at 18:00 LMST.
Figure S6 shows histograms of the 6 marsquake types in an entire Martian year.
Figure S7 gives the simulated ground motion at the receiver of seismic waves in sol 226.
Table S1 presents the detailed numbers of the marsquake events.

Text S1. Solution of 1D heat conduction equation

Surface heat flow estimation provides constraints on the distribution of heat producing radioisotopes and the rate of mantle convection [Barlow, 2014]. In regions where conduction dominates, heat flux (Q) is related to the thermal gradient ($\partial T/\partial z$) by Fourier's Law

$$Q = k\left(\frac{\partial T}{\partial z}\right),$$

where T is temperature and z is depth (downward positive). The thermal conductivity (k) is related to the density (ρ), specific heat (c), and thermal diffusivity (κ) of the ground as below

$$k = \rho c \kappa.$$

The rate at which layers of ground gain or lose heat can be given by

$$\rho c \frac{\partial T}{\partial t} = \frac{\partial Q}{\partial z}.$$

Thus, we can get the heat conduction equation as below

$$\frac{\partial T}{\partial t} = \kappa \frac{\partial^2 T}{\partial^2 z},$$

where $T(z, t)$ is a function of depth (z) and time (t). On the ground surface ($z = 0$), $T(0, t)$ can be described as a sine function

$$T(0,t) = T_0 + A_0 \sin\left(\frac{2\pi}{P} t + \varphi_0\right),$$

where P is the period, T_0 is the average ground temperature in the period, A_0 is the amplitude, and φ_0 is the initial phase. Then the heat conduction equation can be solved as

$$T(z,t) = T_0 + \gamma z + A_0\, e^{-\sqrt{\frac{\pi}{\kappa P}} z} \sin\left(\frac{2\pi}{P} t + \varphi_0 - \sqrt{\frac{\pi}{\kappa P}} z\right),$$

where γ is a constant to describe the vertical gradient of the average temperature, which can be assumed as 0 in regions with low heat flow. At InSight landing site, the heat flow is estimated to be 18 mWm^{-2} [Parro *et al.*, 2017], extremely lower than the heat flow from the solar irradiation. Thus, for simplicity, we assume $\gamma = 0$ in this study.

Since the ground temperature $T(0, t)$ is generally not a perfect sine function, we can replace it by sine series expansion

$$T(0,t) = T_0 + \sum_{i=1}^{n} A_{0i} \sin\left(\frac{2i\pi}{P} t + \varphi_{0i}\right),$$

where i is the order of expansion. Thus, the heat conduction equation can be rewritten as

$$T(z,t) = T_0 + \sum_{i=1}^{n} A_{0i} e^{-\sqrt{\frac{i\pi}{\kappa P}} z} \sin\left(\frac{2i\pi}{P} t + \varphi_{0i} - \sqrt{\frac{i\pi}{\kappa P}} z\right),$$

where n is the number of orders, which is set as 9 in our simulation.

Text S2. Temperature Correction from the Air to the Ground

The air temperature sensors are on the deck of the InSight lander, ~1 m away from the ground. However, the input for the heat conduction simulation is the ground temperature, usually hotter in the daily time and cooler in the nighttime than the air temperature at the altitude of ~1 m. We correct the air temperature (altitude = 1 m) to the ground temperature (altitude = 0 m) according to the modeled air temperature and ground temperature from the Martian Climate Database [Forget *et al.*, 1999] as below:

$$T_{ground}^{\text{Estimated}} = T_{air}^{Recorded} \frac{T_{ground}^{MCD}}{T_{air}^{MCD}},$$

where $T_{ground}^{Estimated}$ is the estimated ground temperature, which is used as temperature boundary for the heat conduction simulation; $T_{air}^{Recorded}$ is the air temperature recorded by InSight; T_{ground}^{MCD} and T_{air}^{MCD} are the ground (altitude = 0 m) and the air (altitude = 1 m) temperatures modeled from MCD, respectively.

Figures S1a and S1b present the MCD temperature as a function of both Solar longitude (Ls) and Local Mean Solar Time (LMST) in the air (altitude = 1 m) and on the ground (altitude = 0 m), respectively. Figures S1c presents an example of the temperature correction for sol 400. Similarly, we estimate the ground temperature sol by sol in all the sols with entire-sol continuous temperature records (Figure S1d).

Text S3. Results of the Subsurface Heat Conduction Beneath InSight

As mentioned in Text S1, the heat conduction equation can describe the thermal process of a given model with several controlling parameters. In our numerical calculations, we use typical values of these parameters obtained from the heating experiments from HP³ [*Grott et al.*, 2021] as follows: soil density ρ = 1211 kg m^{-3}, specific heat c = 630 J kg^{-1} K^{-1}, and thermal conductivity k = 0.039 W m^{-1} K^{-1}. Thus, the thermal diffusivity $\kappa = k/(\rho c)$ at the InSight landing site can be estimated as 5.1×10^{-8} m^2 s^{-1}.

Figure S2a shows the complete numerical solution of daily temperature variation with depth, given the annual average daily temperature as the temperature boundary at $z = 0$. The magnitude of temperature variation decreases with increasing depth at any given time (Figure S2b). The highest subsurface temperature arises with a varying time delay at different depths (Figure S2c). Below the depth of 25 cm (Figure S2b), the temperature is almost stable (i.e., insensitive to heat conduction from solar forcing). This indicates that we can focus on the shallowest 25 cm for analyzing the diurnal variations of subsurface temperature, especially for the shallowest 10 cm, below which daily temperature variations are less than 15 K.

We can see that at the depth of 0 cm (Figure S3a), the temperature starts to rise at 06:00–08:00 and then starts to drop at 17:00–19:00. At the depth of 2 cm (Figure S3b), the temperature starts to rise at 08:00–12:00 and drop at 18:00–20:00. The time delays become larger with increasing depth (Figures S3c-f). Meanwhile, the duration of peak temperature periods (purple) become shorter with depth. The temperature is nearly stable at the depth of 10 cm (Figure S3f) and is totally invariant at the depth of 25 cm (Figure S1b).

Figure S1

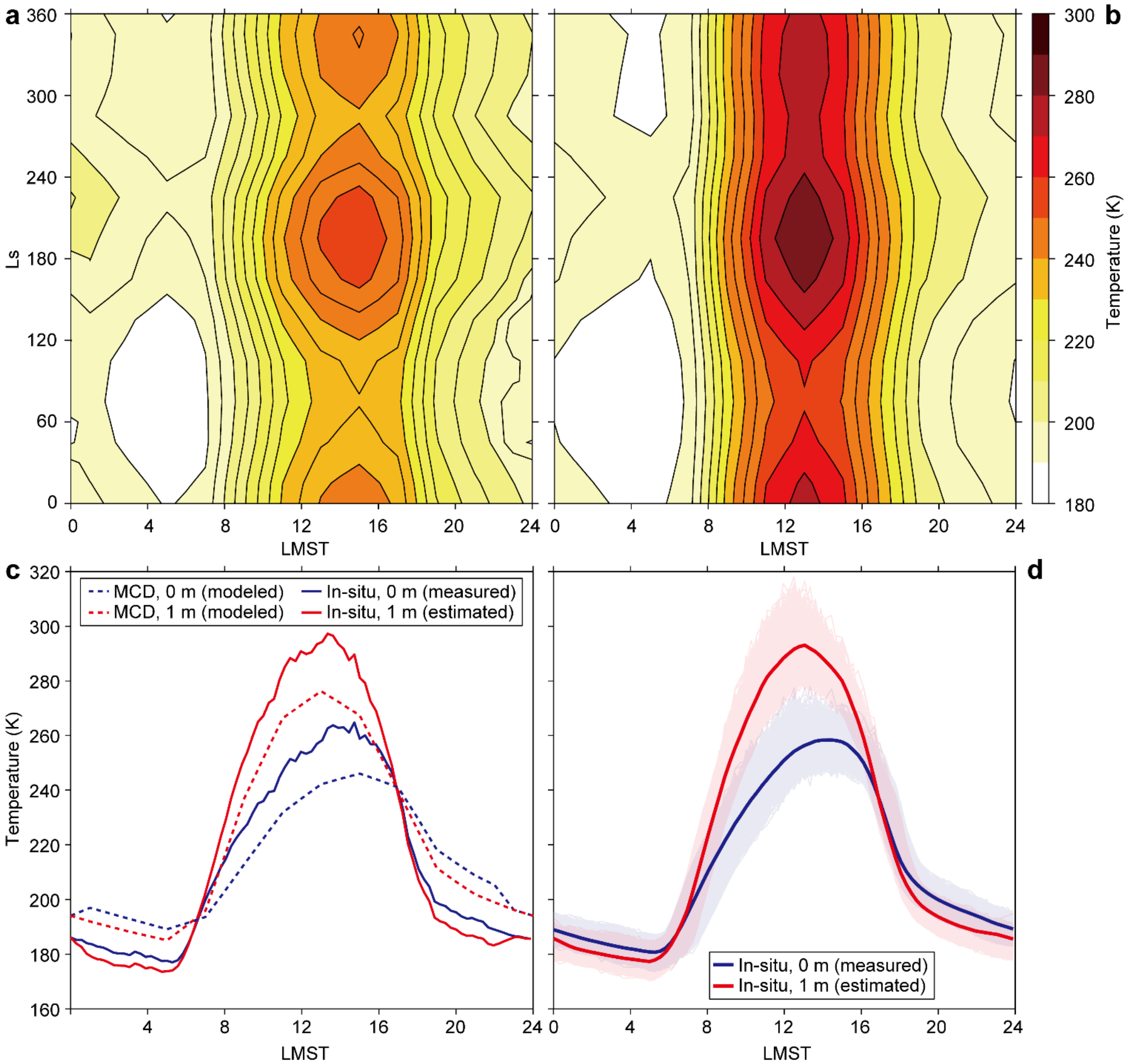

Figure S1. The correction process from air temperature to ground temperature. (a) Air temperature (altitude = 1 m) from MCD. (b) Ground temperature (altitude = 0 m) from MCD. (c) An example of the temperature correction for sol 400. (d) The InSight recorded air temperature (altitude = 1 m) and the estimated ground temperature (altitude = 0 m) after the correction process. The temperature records (semi-transparent blue lines) from the BOOM-Y component of the TWINS (Temperature and Winds for InSight) tip sensor [Spiga et al., 2018] is used in our analysis. Only the sols with entire-sol continuous temperature records are considered. The red and dark blue solid lines denote the average temperatures of these sols, together with the daily records (semi-transparent lines).

Figure S2

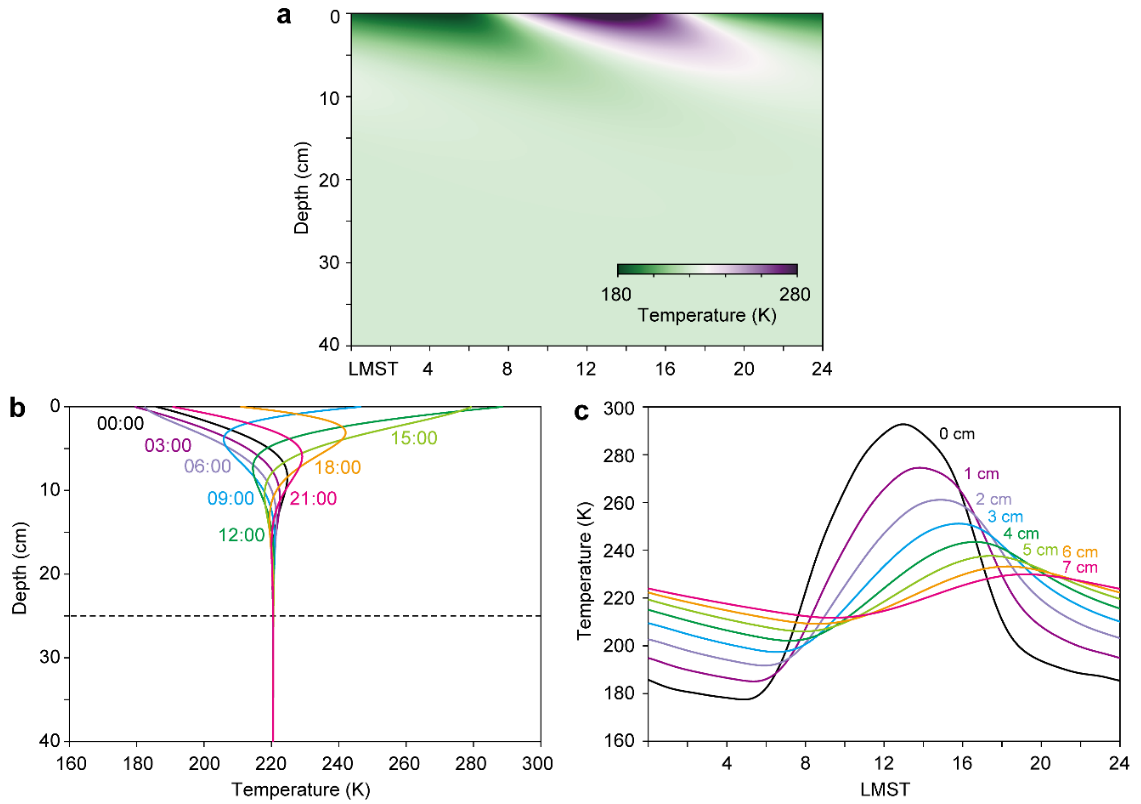

Figure S2. Annually average temperature of the subsurface under the InSight landing site. (a) Temperature as a function of both depth and time of a sol. (b) Temperature as a function of depth at different times of a day. (c) Daily temperature fluctuations at different depths.

Figure S3

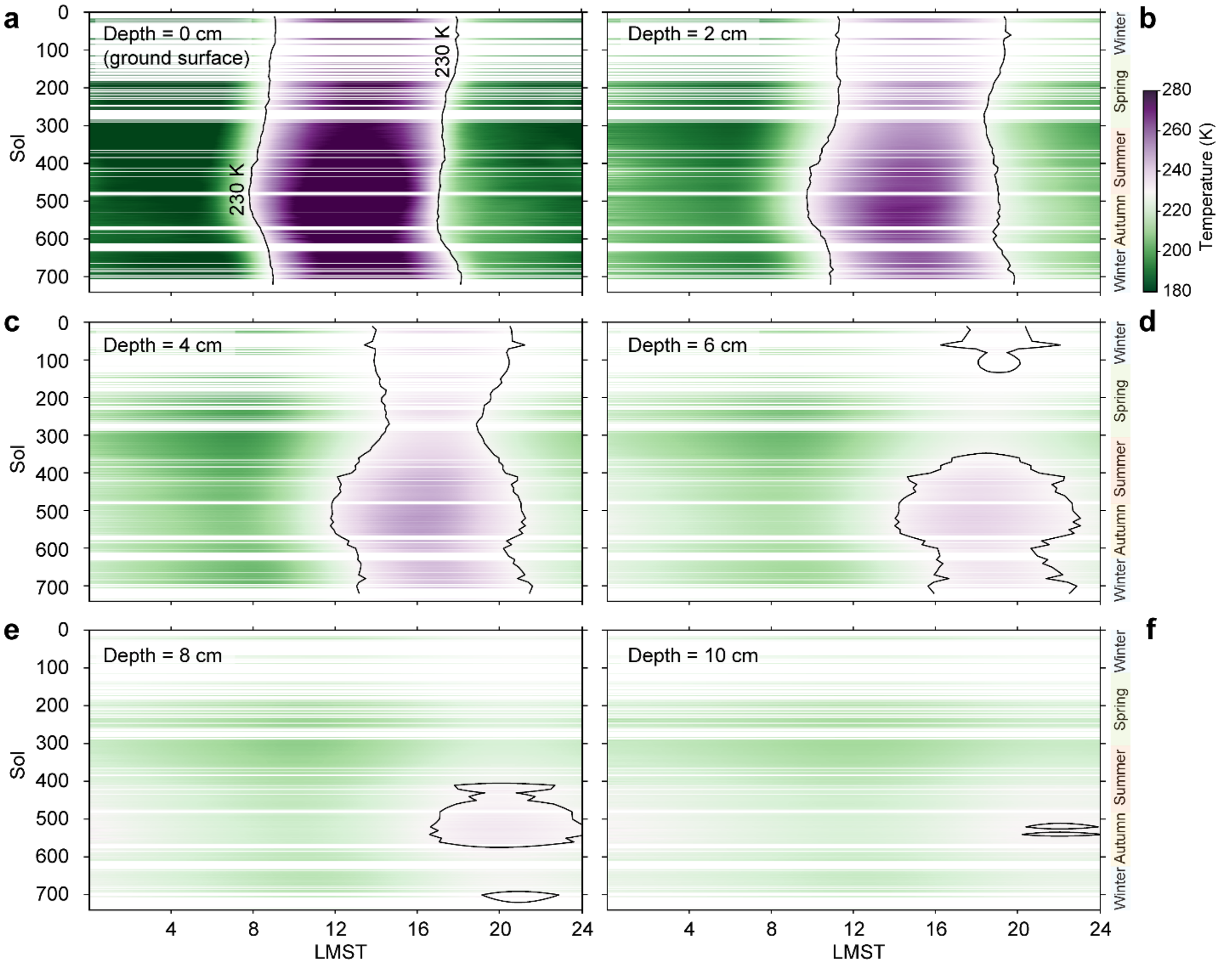

Figure S3. Temperature as a function of both time of day and mission days (sol) at top 10 cm of the subsurface. Horizontal white spaces indicate data gaps due to solar conjunctions or machine stoppages. Black lines denote the isolines of 230 K.

Figure S4

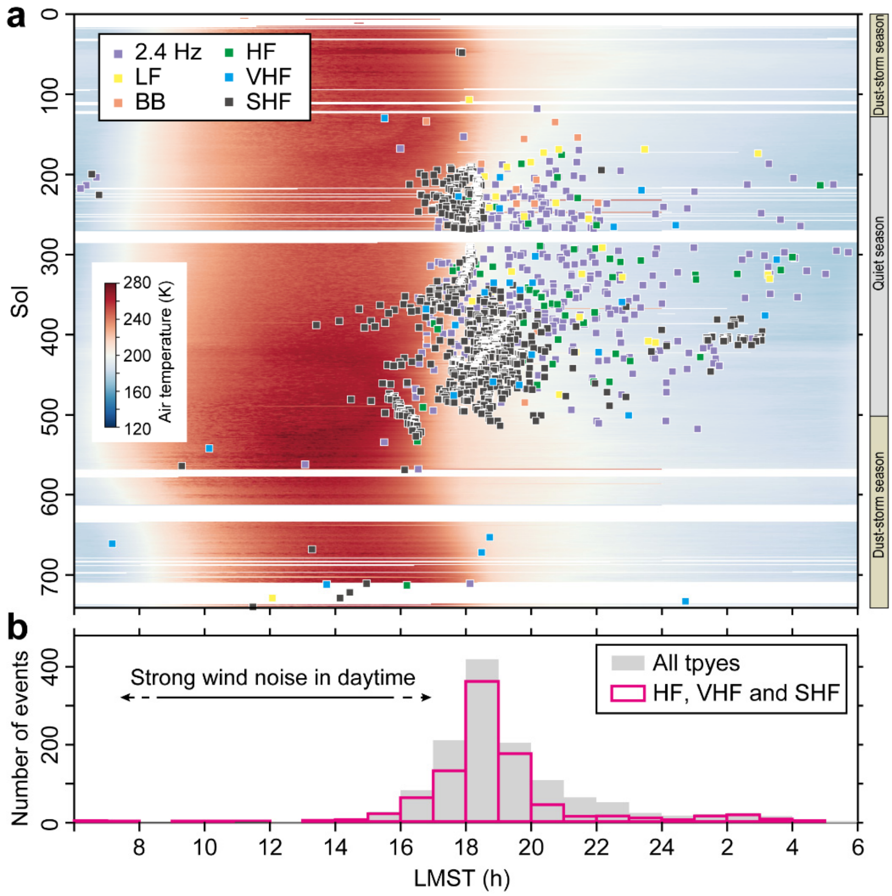

Figure S4. **Phase arrival times of the 6 types of marsquake events and their histogram.** (a) Phase arrival times of the 6 types of marsquake events: 2.4 Hz, broadband (BB), low frequency (LF), high frequency (HF), very high frequency (VHF), and super high frequency (SHF). The background color spectrum is the air temperature centered at sunset. (b) Histogram of marsquake events.

Figure S5

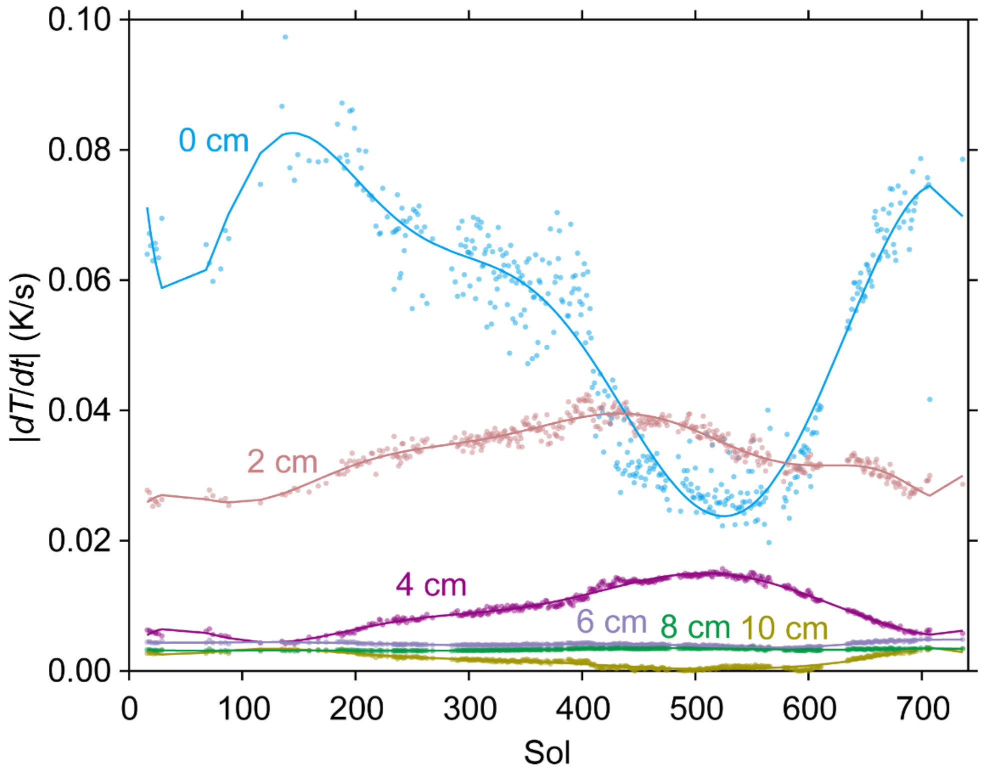

Figure S5. **Calculated absolute temperature variations at different depths on 18:00 LMST.** The dots are calculated values, and the lines are the fitting results.

Figure S6

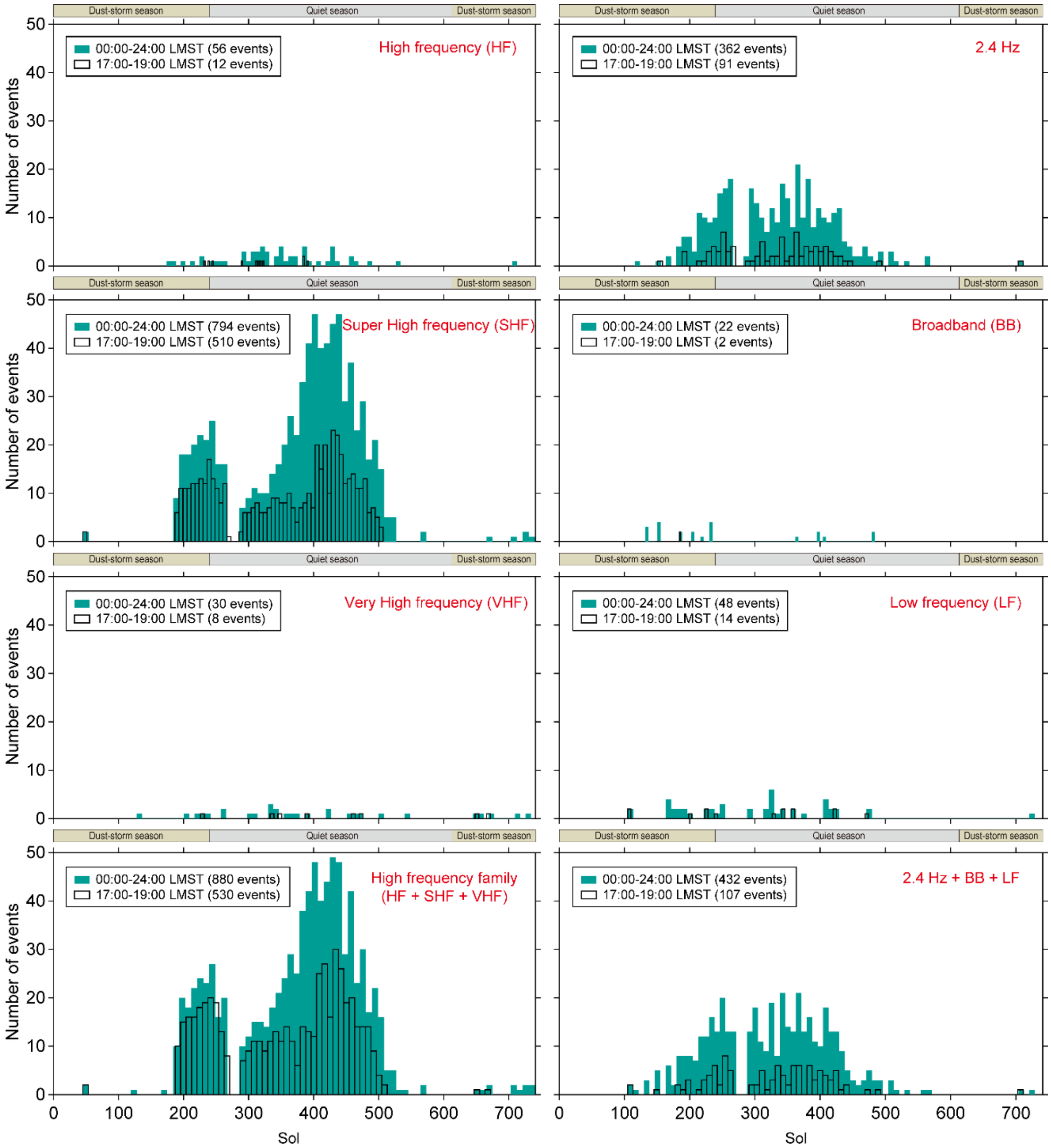

Figure S6. Histograms of the 6 types of marsquake events [*InSight Marsquake Service*, 2021]. Green filled and black framed bars indicate events during 00:00–24:00 and 17:00–19:00 LMST, respectively. Magenta text denotes the types of marsquakes.

Figure S7

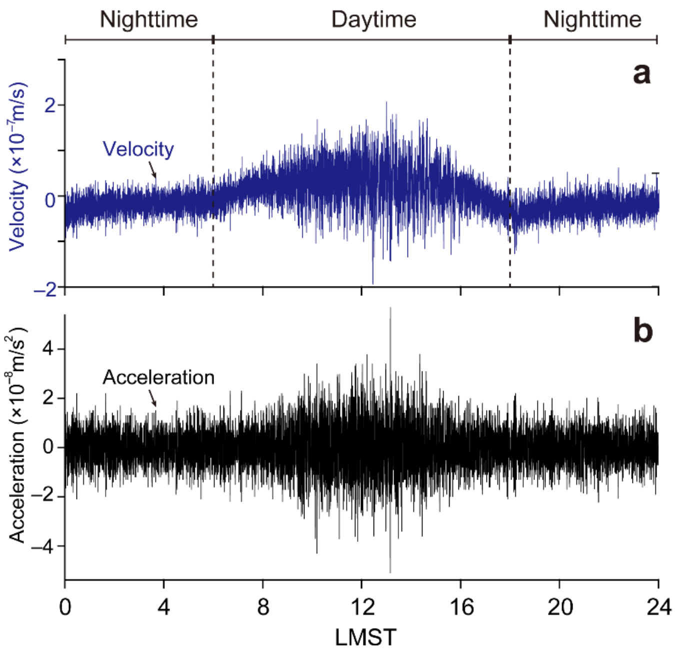

Figure S7. The simulated ground motion at the receiver of seismic waves in sol 226. (a) Vertical velocity. (b) Vertical acceleration.

Table S1. Numbers of different marsquake types [*InSight Marsquake Service*, 2021].

Types	00:00-24:00 (A)	17:00-19:00 (B)	16:00-20:00 (C)	B/A*100%	C/A*100%
High frequency (HF)	56	12	22	21.4%	39.3%
Super high frequency (SHF)	794	510	692	64.2%	87.2%
Very high frequency (VHF)	30	8	14	26.7%	46.7%
2.4 Hz	362	91	157	25.1%	43.4%
Broadband (BB)	22	2	12	9.1%	54.5%
Low frequency (LF)	48	14	21	29.2%	43.8%
HF + SHF + VHF	880	530	728	60.2%	82.7%
2.4 Hz + BB + LF	432	107	190	24.8%	44.0%
HF + SHF + VHF + 2.4 Hz + BB + LF	1312	637	918	48.6%	70.0%

References

InSight Marsquake Service (2021). Mars Seismic Catalogue, InSight Mission; V7 2021-07-01. ETHZ, IPGP, JPL, ICL, Univ. Bristol. https://doi.org/10.12686/a12.

Forget, F., F. Hourdin, R. Fournier, C. Hourdin, O. Talagrand, M. Collins, S. R. Lewis, P. L. Read, and J. P. Huot (1999), Improved general circulation models of the martian atmosphere from the surface to above 80 km, *Journal of Geophysical Research: Planets*, *104*(E10), 24155-24175.

Grott, M., T. Spohn, J. Knollenberg, C. Krause, T. L. Hudson, S. Piqueux, N. Müller, M. P. Golombek, C. Vrettos, and E. Marteau, et al., (2021), Thermal conductivity of the martian soil at the InSight landing site from HP^3 active heating experiments, *Journal of Geophysical Research: Planets*, 126(7), e2021JE006861.

Parro, L. M., Jiménez-Díaz, A., Mansilla, F. & Ruiz, J. Present-day heat flow model of Mars. *Scientific reports* **7**, 1–9 (2017).

Spiga, A., D. Banfield, N. A. Teanby, F. Forget, A. Lucas, B. Kenda, J. A. R. Manfredi, R. Widmer-Schnidrig, N. Murdoch, and M. T. Lemmon (2018), Atmospheric science with InSight, *Space Science Reviews*, *214*(7), 1-64.